Journal of Quantitative Spectroscopy & Radiative Transfer

Precise measurement of pressure broadening parameters for water vapor with a terahertz time-domain spectrometer

Hiromichi Hoshina[a],*, Takamasa Seta[b], Toshiyuki Iwamoto[c], Iwao Hosako[b], Chiko Otani[a], Yasuko Kasai[b]

[a]*RIKEN, 519-1399 Aramaki-Aoba, Aoba-ku, Sendai, Miyagi 980-0845, Japan*
[b]*NICT, 4-2-1 Nukui-Kitamachi, Koganei, Tokyo 184-8795, Japan*
[c]*AISPEC Co., Ltd., 3-17-16, Sennin, Hachioji, Tokyo 193-0835, Japan*

Abstract

The pressure broadening parameters γ_{N_2} and γ_{O_2} of pure rotational transitions of water vapor with nitrogen and oxygen as foreign gases, respectively, were measured with a terahertz time-domain spectrometer (THz-TDS) in the frequency region from 0.5 to 3.5 THz. A White-type multi-pass cell was introduced in the THz-TDS system to precisely measure the absorption spectra of water vapor. The parameters of 36 lines were determined for both N_2 and O_2, of which 25 parameters for γ_{N_2} and 28 parameters for γ_{O_2} were the first laboratory experimental data. The quantum number dependence of the parameters was experimentally observed for the first time due to the good signal-to-noise ratio of this system compared with the conventional Fourier transform infrared spectrometer (FT-IR) experiments.
© 2008 Elsevier Ltd. All rights reserved.

Keywords: Terahertz; THz-TDS; Gas-phase spectroscopy; Water vapor; Pressure broadening parameter

1. Introduction

The development of femtosecond lasers has led to the time-domain spectrometer (TDS) becoming a widespread spectrometry tool in the terahertz (THz) region [1,2]. Since a THz-TDS system detects signals with femtosecond time window and is less affected by thermal noise, it works without liquid helium cooling and enables relatively easy experiments in THz. In addition, the detector has a better signal-to-noise ratio (SNR) and a higher dynamic range (10^6–10^8) than conventional Fourier transform infrared spectrometer (FT-IR) in the 0.3–4.0 THz frequency region, because the THz-TDS system is more stable than the combination of a mercury lamp and a Si bolometer [3]. Due to these advantages, THz-TDS has been recently used for various spectroscopic studies in the THz region [1].

In 1991, H. Harde et al. applied THz-TDS to gas-phase spectroscopy and measured the self-pressure broadening parameters of N_2O molecules. Since then, applicability of THz-TDS to gas-phase spectroscopy

---

has been discussed [4–13]. Because spectral resolution of the THz-TDS is limited to GHz due to the length of the optical delay stage, the experiments using continuous wave sources such as the tunable differential frequency lasers or the backward wave oscillator (BWO) are still advantageous in high-resolution gas-phase spectroscopy [4]. On the other hand, the principles of THz-TDS system lead to the good SNR and large dynamic range below 3 THz [3], and the system allows both strong and weak lines to be measured simultaneously. THz-TDS may show an advantage for the measurement within their frequency resolution, such as the measurements of pressure broadens lines.

Water vapor plays an important role in the Earth's temperature balance. Pressure broadening parameters for water vapor are basic physical parameters to calculate the radiation budget on the Earth. Many measurements have been made for the pressure broadening parameters of the water vapor from the far to the near infrared regions, and are summarized in the HITRAN database [14]. However, data in the 1–5 THz region are not sufficient because there is no optimum method in this frequency region. Consequently, the present data in the HITRAN database in the region was complemented by theoretical values computed by Gamache et al. [15,16].

In this paper, we report the measurement of the pressure broadening parameter of H_2O with a system in which a White-type multi-pass cell is combined with a conventional THz-TDS in the frequency region 0.5–3.0 THz. The pressure broadening parameters γ_{N_2} and γ_{O_2} of pure rotational lines of water vapor were obtained in the pressure of 19–115 and 44–119 kPa, respectively. The obtained parameters were compared with those measured by FT-IR [17] and the theoretical values [15,16]. The accuracy and precision in the system was also examined.

2. Experiment

2.1. THz-TDS setup for gas-phase spectroscopy

The measurement system was built based on a commercial THz-TDS (Aispec: *pulse* IRS-2300) with a White-type multi-pass cell. Fig. 1 shows a schematic diagram and an overview picture of the spectrometer. The outline of the IRS-2300 system is as follows. For the generation and detection of pulsed THz waves,

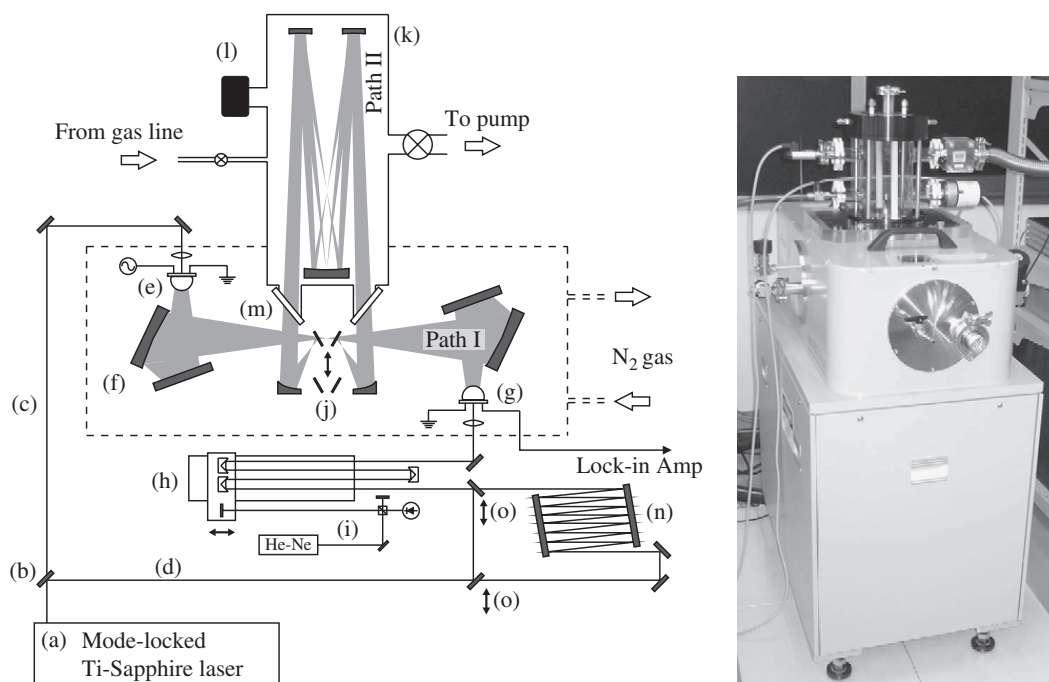Fig. 1. Schematic diagram and overview picture of THz-TDS system: (a) mode-locked Ti:Saphire laser, (b) beam splitter, (c) pump beam, (d) probe beam, (e) photoconductive emitter, (f) elliptical mirror, (g) photoconductive detector, (h) optical delay stage, (i) He–Ne interferometer, (j) flat mirror, (k) gas cell, (l) pressure gauge, (m) polypropylene windows, (n) optical delay path and (o) flat mirrors.

a mode-locked Ti:Sapphire laser (High-Q Laser Co.) with a pulse width of 100 fs, a repetition rate of 80 MHz, and an output power of 200 mW was used. The laser output, (a) in Fig. 1, is divided by a beam-splitter (b) into a pump (c) and a probe beam (d). The pump beam is attenuated to 20 mW and then focused onto the 5 μm gap of a dipole-type GaAs photo-conductive antenna (e) with the applied bias voltage of 37 V. The production and extinction of photocarriers at the antenna causes a single-cycle electric field with a time length of 1 ps, which corresponds to a broadband radiation from 0.1 to 4.5 THz. In the default optical path of the spectrometer (Path I), the THz radiation emerges from the silicon super-hemispherical lens attached to the antenna substrate and is focused by an elliptical mirror (f) to the center of the sample chamber, and then focused again on the other photo-conductive detector antenna (g) with a 5 μm gap. The amplitude of the transmitted THz electric field at the moment when the probe laser pulse reaches the detector is determined from the measurement of the output current caused by the movement of the photocarriers produced by the probe pulse. The bias voltage of the emitter antenna is modulated and the output current from the detector antenna is lock-in amplified after the current amplifier for the detector in order to reduce the low-frequency system noise. The THz time-domain waveform is recorded by changing the time delay of the probe pulse, which is achieved by scanning the optical delay stage (h) whose position is monitored by a co-mounted He–Ne interferometer (i).

A 30-cm-long White-type multipass cell was designed and built so as to fit the default optical path, Path I, of the IRS-2300 system. The cell was attached on the top of a vacuum chamber (see the photograph in Fig. 1). By the insertion of two flat mirrors (j), the THz wave was reflected into the multi-pass cell (k) (Path II). The introduced THz beam was reflected 7 times by gold spherical mirrors, and the total path length is about 2.05 m. The cell was made of PYREX®, and four NW-25 vacuum ports were attached on the sidewall. The pressure in the cell is monitored by a capacitance manometer (MKS Baratron®) (l). The cell was sealed with o-rings and 2-mm-thick polypropylene windows (m) glued at the entrance and exit of the THz beam. Since the dipole radiation from the antenna is totally polarized, the reflection from the window was minimized by tilting the windows at the Brewster's angle of 54°. A time delay unit (n) is inserted into the probe beam path by moving a pair of mirrors (o) in order to compensate the path length of the probe pulse with that of THz beam passing through the gas cell. The mirrors (j) and (o) are controlled by a PC to switch between paths I and II. The sample chamber (enclosed by a dashed line in Fig. 1) surrounding the THz path is purged by a continuous flow of nitrogen gas to minimize water vapor of the path outside the gas cell.

The optical delay stage (h) is scanned over a range of 82.9 mm producing a change in the optical delay of 332 mm. This length corresponds to a frequency resolution of 1.0 GHz. The signal is recorded every 0.316 μm triggered by the fringes of the He–Ne interferometer. The stage moves at 0.6 mm/s and takes about 2 min for a single scan. In our experiments, multiple scans (*n* times) are applied and the time-domain waveforms are averaged over the scans.

2.2. Fourier transform and the absorbance spectra

The observed time-domain waveforms are Fourier transformed (FT) to the frequency-domain spectra. Before FT, zero values are added at the end of the time-domain waveforms in order to complement the points in the frequency domain spectra. This method is the same as the "zero-filling" technique of FT-IR spectroscopy [18]. We added seven times zero-filling data at the end of the observed waveform, and thus the total length becomes eight times of the observed one. No apodization function was applied.

The absorbance of the sample $\alpha(\omega)$ was obtained as

$$\alpha(\omega) = -\log_{10}(I_{sa}(\omega)/I_{ref}(\omega)) \tag{1}$$

where $I_{sa}(\omega)$ was the sample spectrum and $I_{ref}(\omega)$ was the reference spectrum. The reference spectrum was first measured and then the sample spectrum. The stability of the THz-TDS system is experimentally examined as discussed in the last section.

2.3. Frequency calibration

The frequency calibration was performed using the center peak positions of the rotational lines of pure water vapor at the pressures of 10 Pa. The peak positions were obtained from the center frequency in the
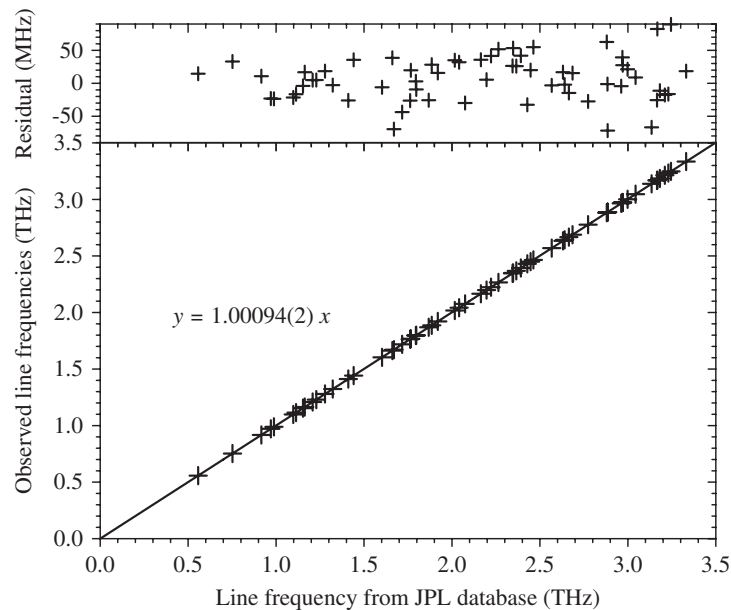
Fig. 2. Linear fitting between the observed transition frequency and the values from the NASA-JPL spectroscopic catalog [20] for the rotational lines of water vapor. The upper graph shows the residuals of the least-squares fitting.

spectral fitting by a Lorentzian function to the peaks. Note that the pressure shift of the center frequency is typically less than a few MHz in our pressure conditions and is much smaller than the uncertainty of the obtained frequency as shown below [19]. In total, 81 lines in the range from 0.5 to 3.5 THz were used in the calibration. The center peak positions of each line were compared to the known transition frequencies from the NASA-JPL spectroscopic catalog [20]. Fig. 2 shows the relationship and the result of a linear fitting between the observed transition frequencies and the values from the NASA-JPL spectroscopic catalog. The upper graph in Fig. 2 shows the residuals of the least-squares fitting. The frequencies of the spectrometer were calibrated from fitting as

$$f' = 1.00094(2)f \tag{2}$$

where f' is the observed frequency and f is the frequency based on the NASA-JPL data. The accuracy of the frequencies of THz-TDS mainly comes from the accuracy of the position of the optical delay stage ((h) in Fig. 1) monitored by the He–Ne interferometer. The calibrated frequencies were used for the measurements of pressure broadening parameters.

2.4. Measurement of THz absorption spectra of water vapor

The pressure broadening parameters were obtained from the pressure dependence of the rotational line shape of water vapor mixed with a foreign gas (N_2 or O_2). A reference spectrum was first measured using the vacuum cell evacuated below 10^{-5} Pa by a turbo molecular pump. The reference spectrum was obtained by the averaging of 100 scans. Then, the water vapor was introduced via a vacuum line. The partial pressure of the water vapor was set to 250 Pa, at which the most of the rotational lines can be observed without saturation. In the measurements, the partial pressure of the water vapor might vary gradually due to the adsorption on the surface of the cell. To minimize the effect, the water vapor of about 500 Pa was first introduced into the cell, and the cell was left for 30 min to wait for the pressure to reach the equilibrium, and then the pressure was adjusted to 250 Pa by pumping. Subsequently, N_2 (99.9999%) or O_2 (99.9999%) was added until the total pressure reached the experimental condition. Six conditions for the total pressure for each foreign gas (from 19.3 to 115.2 kPa for N_2 and 44.0 to 118.5 kPa for O_2, respectively) were used. The change of the total pressure was less than 0.1 kPa during the measurement time of 1 hour. The cell and the spectrometer were

placed at room temperature of $T = 22 \pm 1\,°C$ during the measurements. In the THz-TDS measurements, 50 scans were applied and the averaged time profiles are used to derive the spectra.

3. Results

3.1. The least-squares fitting of the rotational line shape

The rotational lines of water vapor mixed with nitrogen and oxygen gas were fitted with a Lorentzian line shape function. Fig. 3 shows examples of the observed absorption spectra of H_2O with N_2, the result of non-linear least-squares fitting and the residuals. The upper trace shows the $2_{02} \leftarrow 1_{11}$ and the lower trace shows the $3_{12} \leftarrow 3_{03}$ and $1_{11} \leftarrow 0_{00}$ rotational transitions. The pressure of H_2O was 250 Pa and the pressure of N_2 was 19.3 kPa. A data subset with the width of about 0.1 THz was taken for each fit.

Some intense transitions, such as $3_{12} \leftarrow 3_{03}$ in Fig. 3, do not fit with a Lorentzian curve around the peak top. When the absorbance α is too strong, the signal of the sample spectrum I_{sa} is depleted and it is difficult to overcome the system noise. In such cases, the data-points with higher absorbance are not reliable, and should not be used for the fitting. We decided to remove data with higher absorbance (more than 3 for example), and fit only with the tails of the line shape. To find the appropriate threshold for data cutting, the fitting procedure was repeated by removing data-points one by one until the obtained parameters stabilized. We rejected very strong lines ($2_{21} \leftarrow 1_{10}$ at 2773.80 GHz and $4_{14} \leftarrow 3_{03}$ at 2640.32 GHz, for example), whose parameters were diverging due to the lack of data-points.
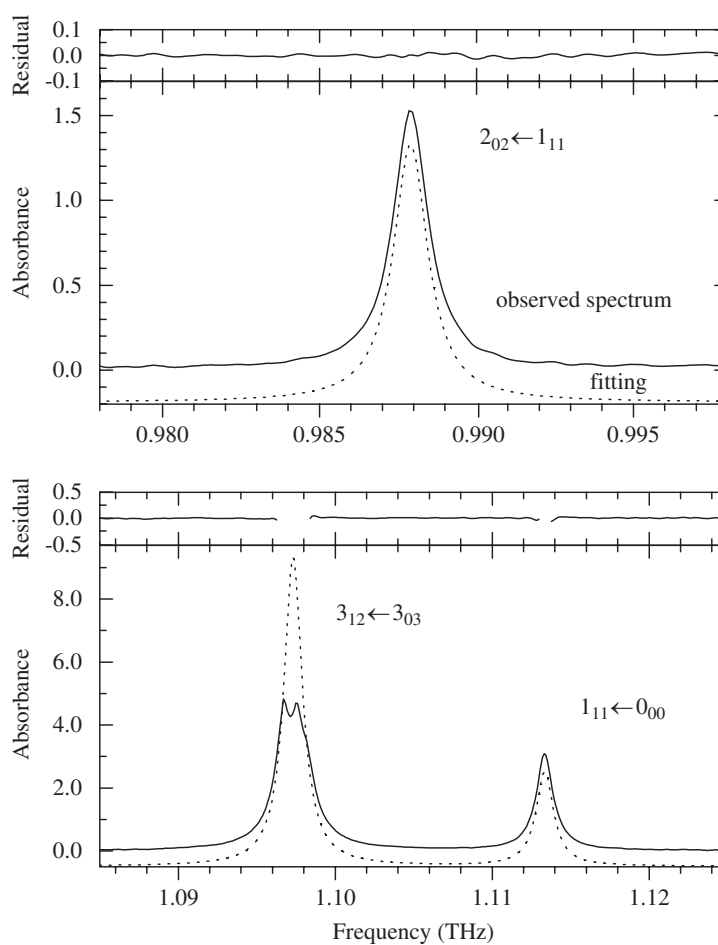
Fig. 3. Observed absorption spectra of H_2O with N_2 (solid line), the result of non-linear least-squares fitting (dashed line) and the residuals. The dashed lines are shifted by -0.2 for upper trace and -0.5 for lower trace, respectively, to make ease to show the difference. The upper trace shows the $2_{02} \leftarrow 1_{11}$ and the lower trace shows the $3_{12} \leftarrow 3_{03}$ and $1_{11} \leftarrow 0_{00}$ rotational transitions. The pressure of H_2O is 250 Pa and the pressure of N_2 is 19.3 kPa.

In the case, where neighboring lines overlapped, the line shapes were fitted using linear combinations of Lorentzian functions. However, when the lines were too close, such as lines $2_{21} \leftarrow 2_{12}$ and $2_{12} \leftarrow 1_{01}$ at 1660.96 and 1669.74 GHz, respectively, the fitting does not converge, and we rejected them also.

As seen in the fitting residuals in Fig. 3, the observed line shape was well fitted by a Lorentzian function. We did not use Voight and van Vleck Weiscopf line functions for the line shape fitting due to the following reasons. First, the Doppler broadening width of water vapor at 300 K is negligible ($\sim$10 MHz) [19] compared to our resolution of $\Delta f = 1$ GHz. Moreover, no significant difference was found between those from the van Vleck Weisskopf functions and the Lorentzian functions, because of our measurement conditions, $\Delta f < 0.01 f$ [19].

The obtained fitting parameters for the $1_{10} \leftarrow 1_{01}$, $2_{11} \leftarrow 2_{02}$, $2_{02} \leftarrow 1_{11}$, $3_{12} \leftarrow 3_{03}$ and $1_{11} \leftarrow 0_{00}$ transitions in different pressure conditions are summarized in Table 1. The integrated intensity α, transition frequency f, and line width Δ are shown. The values in the parenthesis show the standard deviation of the fitting. In the table, the increase of the integrated intensity with the pressure was seen and we will discuss it in the next section. There was no significant shift of the center frequency of each transition, and the pressure shift was much smaller than the accuracy of the obtained frequency.

3.2. The pressure broadening parameter

The pressure broadening parameters γ_{N_2} and γ_{O_2} were obtained as the slope of the linear fitting of the half-width at half-maximum (HWHM) as a function of the pressure. Before plotting the line widths, we should first check the resolution limit of the measurements. Since no apodization function was used for FT, the spectral line shape was obtained as the convolution of the real line shape and a sinc window function. Assuming that the transition is homogeneous, the time-domain waveform can be described as a slowly damping oscillation [21]. The Fourier transformed line function obtained in the finite time window is written as

$$F(\omega) \propto \left| \int_0^T e^{-2\pi\Delta v t} \cos(2\pi v_0 t) e^{-i\omega t} \, dt \right|^2 \tag{3}$$

where ω is frequency, t is time, v is the resonance frequency, Δv is the real width of the line in HWHM in the Lorentzian function, and T is the measurement time window of the spectrometer. The frequency resolution of the spectrometer is $\Delta f = 1$ GHz, which corresponds to a measurement time window of $T = 1$ ns. When the observed line width is smaller than the frequency resolution, the line shape described in Eq. (3) is different from the Lorentzian line shape. We calculated the line shapes in Eq. (3) numerically and plotted the ratio of the obtained HWHM values in the fittings by a Lorentzian function to the real line width, Δv, as a function of the ratio of Δf to Δv in Fig. 4. The plot shows that as the resolution of the spectrometer becomes greater, the observed line shape gets distorted from the Lorentzian line shape and the line width becomes broader than the real one. This effect becomes important when the real line width is narrower, i.e., the pressure is lower. For example, at the lowest pressure of N$_2$ at 19.3 kPa, the observed HWHM of the $2_{02} \leftarrow 1_{11}$ rotational transition was 0.65 ± 0.01 GHz. From the ratio of $\Delta f/\Delta v \sim 1.5$, the HWHM/$\Delta v$ was estimated to be 1.02 from the above calculation. Using this factor, we corrected the obtained HWHM to 0.66 ± 0.01 GHz. Thus, all of the obtained line widths were corrected when they were below the resolution of the spectrometer. In reality, the correction was only effective at the lowest pressure for N$_2$ and O$_2$ in our experiments, because the obtained line widths were greater than $\Delta f = 1$ GHz for other pressure conditions. Note also that the error due to this correction is expected to be negligible (much less than 1% in HWHM) compared with the ones in the spectral fittings. This means that the correction errors do not affect the following results.

Based on these considerations, the pressure broadening parameters γ_{N_2} and γ_{O_2} of each line were obtained by the least-squares fitting of the obtained line widths with a linear function of the pressure conditions. As an example, Fig. 5 shows two plots of the observed HWHM for the $1_{10} \leftarrow 1_{01}$ rotational transition as a function of the pressure of N$_2$ and O$_2$. The slope corresponds to the pressure broadening parameter of the line due to the foreign gas, and the intercept at zero pressure corresponds to the self-pressure broadening line width and Doppler broadening line width of the water molecule. Pressure broadening parameters of 36

Table 1
The integrated line intensity α, the transition frequency f, and the line width Δ obtained by the least-squares fitting with a Lorentzian line shape function

	19.3 kPa	38.7 kPa	56.0 kPa	75.8 kPa	95.6 kPa	115.2 kPa
H_2O (250 Pa) + N_2						
556.92 ($1_{10} \leftarrow 1_{01}$)						
α (GHz)	6.61(3)	7.84(3)	8.26(4)	8.32(4)	9.13(5)	9.29(6)
f (GHz)	556.97(0)	557.05(1)	557.07(1)	557.06(1)	557.07(2)	557.23(3)
Δ (GHz)	0.72(1)	1.35(1)	1.96(2)	2.58(3)	3.30(4)	3.99(5)
752.02 ($2_{11} \leftarrow 2_{02}$)						
α (GHz)	4.48(2)	5.26(3)	5.60(3)	5.73(4)	6.03(5)	6.46(6)
f (GHz)	752.07(0)	752.10(1)	752.14(1)	752.16(2)	752.19(3)	752.18(4)
Δ (GHz)	0.67(1)	1.32(2)	1.89(2)	2.56(4)	3.18(6)	3.93(7)
987.85 ($2_{02} \leftarrow 1_{11}$)						
α (GHz)	3.22(3)	3.76(3)	4.15(4)	4.32(3)	4.69(3)	4.78(5)
f (GHz)	987.90(0)	987.90(1)	987.88(1)	987.86(1)	987.82(2)	987.75(3)
Δ (GHz)	0.65(1)	1.28(2)	1.88(5)	2.52(5)	3.12(5)	3.86(9)
1097.28 ($3_{12} \leftarrow 3_{03}$)						
α (GHz)	21.3(3)	24.7(2)	26.2(2)	26.7(1)	26.9(1)	27.9(1)
f (GHz)	1097.32(0)	1097.44(1)	1097.52(1)	1097.53(1)	1097.53(1)	1097.60(2)
Δ (GHz)	0.71(1)	1.32(1)	1.87(2)	2.50(2)	3.16(2)	3.29(2)
1113.26 ($1_{11} \leftarrow 0_{00}$)						
α (GHz)	6.6(1)	7.6(1)	8.3(1)	8.5(2)	8.9(2)	9.4(3)
f (GHz)	1113.40(2)	1113.45(2)	1113.43(2)	1113.38(3)	1113.36(4)	1113.41(5)
Δ (GHz)	0.66(1)	1.31(1)	1.91(2)	2.59(3)	3.32(3)	3.90(4)
	44.0 kPa	58.9 kPa	75.3 kPa	90.8 kPa	104.2 kPa	118.5 kPa
H_2O (250 Pa) + O_2						
556.92 ($1_{10} \leftarrow 1_{01}$)						
α (GHz)	4.00(1)	4.67(2)	4.91(2)	5.04(3)	5.07(3)	5.05(4)
f (GHz)	556.98(0)	556.99(0)	557.01(1)	557.05(1)	557.01(1)	557.07(1)
Δ (GHz)	0.86(1)	1.10(1)	1.38(2)	1.67(3)	1.89(3)	2.14(4)
752.02 ($2_{11} \leftarrow 2_{02}$)						
α (GHz)	2.65(1)	3.09(2)	3.29(2)	3.18(3)	3.24(3)	3.24(4)
f (GHz)	752.06(0)	752.08(0)	751.11(1)	752.13(1)	752.13(1)	752.16(2)
Δ (GHz)	0.86(1)	1.10(2)	1.39(3)	1.60(4)	1.81(5)	2.02(6)
987.85 ($2_{02} \leftarrow 1_{11}$)						
α (GHz)	1.97(1)	2.33(1)	2.43(1)	2.52(2)	2.54(2)	2.54(2)
f (GHz)	987.95(0)	987.96(0)	987.96(1)	988.00(1)	987.97(1)	988.00(1)
Δ (GHz)	0.86(1)	1.12(2)	1.37(2)	1.66(3)	1.86(3)	2.08(4)
1097.28 ($3_{12} \leftarrow 3_{03}$)						
α (GHz)	12.8(1)	14.2(1)	15.6(1)	16.3(1)	16.5(1)	16.2(1)
f (GHz)	1097.41(1)	1097.40(3)	1097.42(0)	1097.49(1)	1097.47(1)	1097.55(1)
Δ (GHz)	0.91(1)	1.14(1)	1.35(1)	1.56(1)	1.76(1)	1.99(1)
1113.26 ($1_{11} \leftarrow 0_{00}$)						
α (GHz)	4.0(1)	4.6(0)	4.9(1)	5.0(1)	5.0(1)	5.0(1)
f (GHz)	1113.45(2)	1113.37(1)	1113.41(1)	1113.46(2)	1113.42(2)	1113.43(4)
Δ (GHz)	0.84(1)	1.10(1)	1.40(1)	1.68(3)	1.92(2)	2.17(3)

The parameters of the transitions of $1_{10} \leftarrow 1_{01}$, $2_{11} \leftarrow 2_{02}$, $2_{02} \leftarrow 1_{11}$, $3_{12} \leftarrow 3_{03}$ and $1_{11} \leftarrow 0_{00}$ are shown in different pressure conditions.

transitions were obtained for both N_2 and O_2. The resulting parameters are shown in Table 2 along with their standard deviations. The standard deviations of the parameters were about 1% for transitions with good SNR.
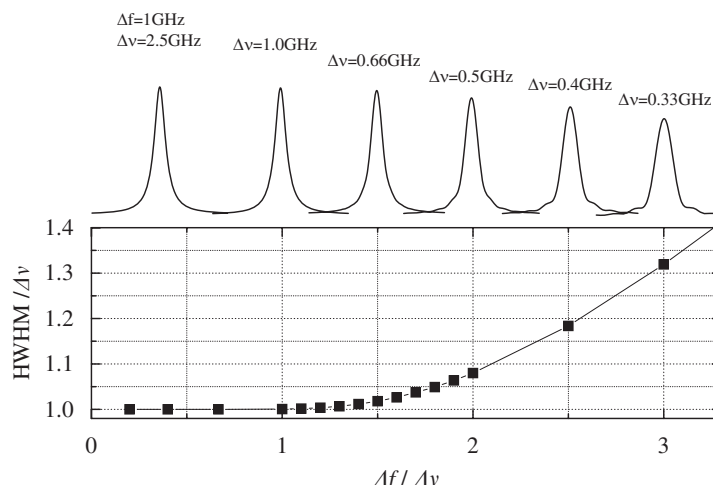
Fig. 4. The change of line shape with spectral resolution. The upper traces show the calculated line shape for $\Delta v = 2.5, 1.0, 0.66, 0.5, 0.4, 0.33$ GHz by assuming the system resolution as $\Delta f = 1$ GHz. The lower plot shows the obtained HWHM by fitting the calculated line shape with a Lorentzian function.
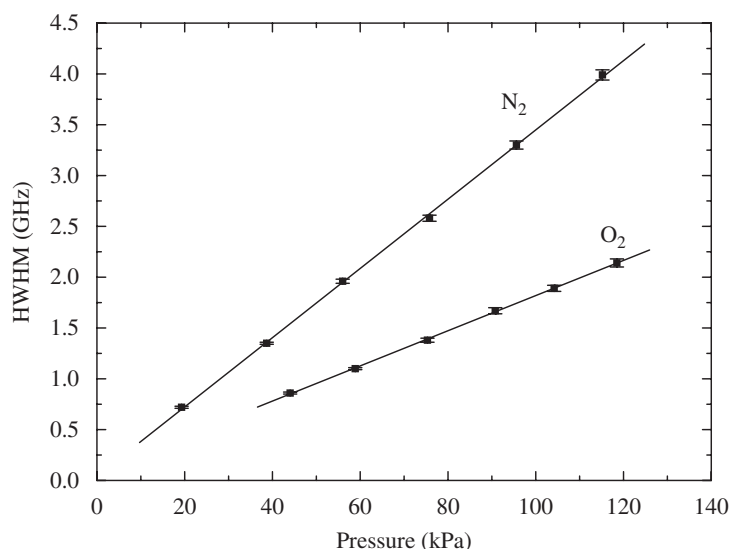

Fig. 5. Examples of the pressure broadened line width for the $1_{10} \leftarrow 1_{01}$ rotational transition of H_2O as a function of the pressure of N_2 and O_2. The error bars indicate 1 sigma limits. The linear least-squares fitting to the data is given by a solid line.

4. Discussion

4.1. Comparison of the parameters with other works

The pressure broadening parameters obtained by FT-IR [17] are listed in the fourth and seventh columns of Table 2. The parameters of 11 lines were obtained for γ_{N_2} and 10 lines for γ_{O_2} in Ref. [17]. In addition, 25 parameters of γ_{N_2} and 28 parameters of γ_{O_2} were obtained for the first time by our measurement. Compared to the FT-IR data, the number of parameters is about three times larger and the standard deviations were about five times smaller. The higher precision of this work is mainly due to the better SNR of the THz-TDS. As discussed in Ref. [3], a THz-TDS has a potential to achieve a better SNR than FT-IR below 3.0 THz, because the femto second laser is more stable than the mercury lamp and the Si bolometer used in FT-IR.

The pressure broadening parameters of water vapor and its isotopomers were theoretically calculated by Gamache et al. [15]. The complete tables of parameters were released on their website [16], and a part of them

Table 2
The obtained γ_{N_2} and γ_{O_2}

Observed frequency (GHz)	$J'_{K'_a,K'_c} \leftarrow J''_{K''_a,K''_c}$ [19]	γ_{N_2} (MHz/kPa)			γ_{O_2} (MHz/kPa)		
		This work	FT-IR [16]	Calc. [15]	This work	FT-IR [16]	Calc. [15]
556.92	$1_{1,0} \leftarrow 1_{0,1}$	33.58(27)		35.93	16.96(33)		15.11
752.02	$2_{1,1} \leftarrow 2_{0,2}$	33.38(36)	31.2(27)	34.17	16.02(48)		14.66
987.85	$2_{0,2} \leftarrow 1_{1,1}$	32.90(48)	33.2(35)	33.96	16.58(39)	12.7(13)	14.67
1097.28	$3_{1,2} \leftarrow 3_{0,3}$	32.32(29)	34.2(8)	32.71	14.10(11)	14.1(38)	13.60
1113.26	$1_{1,1} \leftarrow 0_{0,0}$	34.33(25)	27.5(16)	33.78	17.87(29)	17.08(86)	14.64
1153.06	$3_{1,2} \leftarrow 2_{2,1}$	34.43(52)	29.2(40)	32.15	19.32(49)	15.4(27)	13.48
1162.86	$3_{2,1} \leftarrow 3_{1,2}$	27.72(30)	32.7(8)	31.72	11.85(10)	12.87(45)	13.26
1207.58	$4_{2,2} \leftarrow 4_{1,3}$	31.44(21)	30.4(13)	31.61	14.44(21)	11.90(59)	12.81
1228.73	$2_{0,2} \leftarrow 2_{1,1}$	31.51(24)	32.0(13)	32.71	15.75(28)	16.38(72)	13.85
1321.99	$6_{2,5} \leftarrow 5_{3,2}$	28.2(11)		27.95	12.62(88)		11.3
1410.51	$5_{2,3} \leftarrow 5_{1,4}$	30.98(17)	32.8(7)	31.30	12.60(08)	12.60(50)	12.35
1541.91	$6_{3,3} \leftarrow 5_{4,2}$	34.4(90)		27.61	10.0(30)		11.12
1602.12	$4_{1,3} \leftarrow 4_{0,4}$	31.43(22)		31.82	15.80(9)		12.85
1716.63	$3_{0,3} \leftarrow 2_{1,2}$	27.8(13)		32.61	18.30(60)		13.51
1761.92	$6_{3,3} \leftarrow 6_{2,4}$	38.05(84)		30.20	12.72(50)		11.98
1867.62	$5_{3,2} \leftarrow 5_{2,3}$	24.34(30)		30.08	11.67(16)		12.05
2015.91	$8_{3,5} \leftarrow 8_{2,6}$	26.2(17)		29.68	11.34(66)		11.49
2040.40	$4_{3,1} \leftarrow 4_{2,2}$	29.64(19)		29.85	13.55(8)		12.21
2074.29	$4_{1,3} \leftarrow 3_{2,2}$	31.83(29)		31.41	14.46(14)		12.78
2164.04	$3_{1,3} \leftarrow 2_{0,2}$	32.59(84)		33.55	14.80(28)		13.78
2196.23	$3_{3,0} \leftarrow 3_{2,1}$	27.87(58)		29.47	13.93(29)		12.36
2221.67	$5_{1,4} \leftarrow 5_{0,5}$	27.90(83)		30.02	13.11(26)		12.03
2264.07	$4_{2,3} \leftarrow 4_{1,4}$	29.70(75)		30.23	13.84(46)		12.39
2317.64	$9_{4,5} \leftarrow 9_{3,6}$	26.9(42)		28.81	11.6(15)		11.27
2344.15	$7_{2,5} \leftarrow 7_{1,6}$	23.77(48)		27.72	12.57(17)		11.11
2365.80	$3_{3,1} \leftarrow 3_{2,2}$	26.06(47)		29.13	14.82(20)		12.26
2391.48	$4_{0,4} \leftarrow 3_{1,3}$	29.8(14)	30.6(72)	31.42	11.85(41)		12.73
2428.08	$9_{3,6} \leftarrow 9_{2,7}$	26.9(30)		27.35	11.54(71)		10.92
2446.73	$8_{4,4} \leftarrow 8_{3,5}$			28.84	10.9(12)		11.26
2462.85	$4_{3,2} \leftarrow 4_{2,3}$	28.17(99)	32.9(22)	28.33	12.83(33)		11.80
2567.04	$7_{3,4} \leftarrow 6_{4,3}$	28.8(22)		28.01	12.14(81)		10.98
2664.41	$7_{4,3} \leftarrow 7_{3,4}$			28.56		12.26(63)	11.10
2685.51	$5_{2,4} \leftarrow 5_{1,5}$			27.51		14.90(54)	11.44
3210.16	$7_{3,5} \leftarrow 7_{2,6}$	23.2(16)		22.55	10.20(71)		9.83
3229.96	$6_{4,3} \leftarrow 6_{3,4}$	19.4(11)		23.77	6.76(30)		10.23
3331.29	$3_{2,2} \leftarrow 2_{1,1}$	42.8(19)		32.62	16.3(14)		13.56
3494.90	$8_{4,5} \leftarrow 8_{3,6}$	15.3(17)		21.13	8.17(63)		9.40
3509.27	$9_{5,4} \leftarrow 9_{4,5}$	22.4(98)		25.66			10.06
3536.72	$7_{1,6} \leftarrow 7_{0,7}$	22.08(75)		22.71	9.73(34)		10.03

The first and second columns show the center frequency of the lines (calibrated) and the assignment based on the JPL catalogue [20]. The other column shows the pressure broadening parameters γ_{N_2} and γ_{O_2} obtained by this work, FT-IR measurements [17] and calculation [15,16]. In the parentheses the value of one deviation of the parameters is given.

is included in Table 2. Fig. 6 shows the parameters obtained by (a) this work, (b) FT-IR measurement [17] and (c) calculation [15,16] as a function of energy-ordered index, $J(J+1)+Ka-Kc+1$ [15]. In the calculated values, the quantum number dependence of the parameters is clearly seen. The parameters show a tendency to decrease at higher quantum numbers. A similar clear dependence on the quantum number is also seen in our results, but not confirmed by FT-IR because of its uncertainty. Fig. 7 shows the correlation plot between the calculated parameters and the experimental values. The parameters obtained by THz-TDS show a strong correlation with the theoretical values. This is the first result that gives an experimental value of the quantum number dependence of these parameters in the 0.5–3.0 THz region. As shown in Figs. 6 and 7, the quantum number dependence of the obtained parameters is stronger than the theoretical prediction. We expect that our
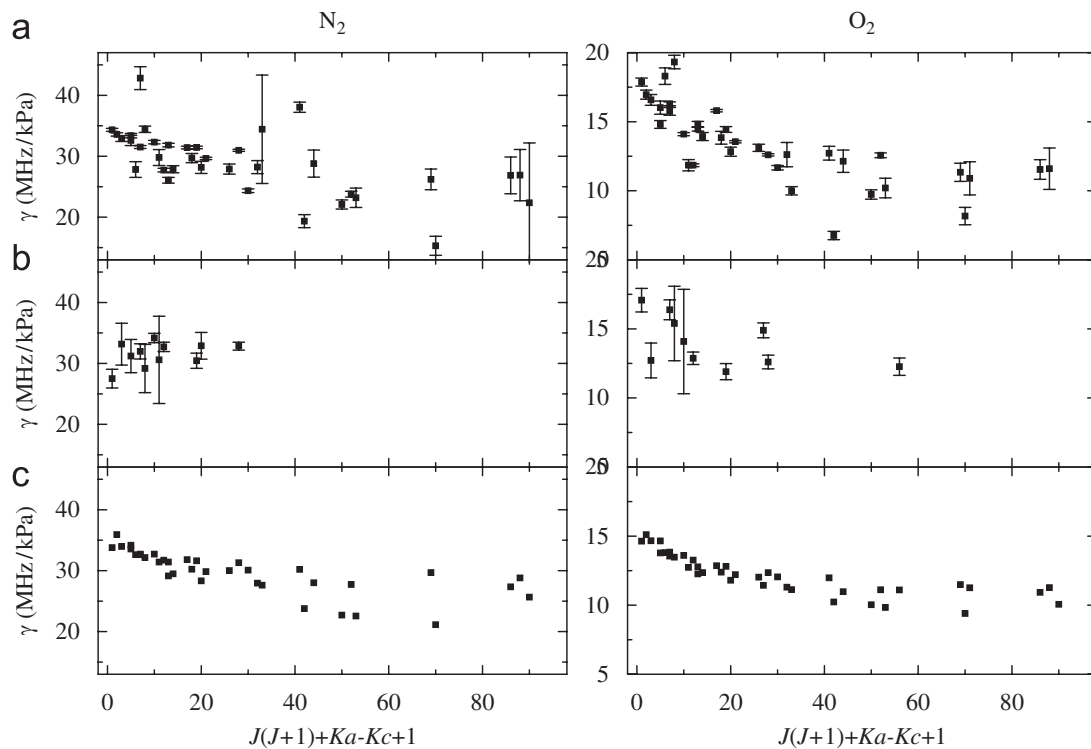
Fig. 6. The pressure broadening parameters γ_{N_2} and γ_{O_2} obtained by (a) this work, (b) FT-IR measurements [16] and (c) calculation [15,16] versus an energy-ordered index, $J(J+1)+Ka-Kc+1$. The error bar shows the statistical error (1 sigma).
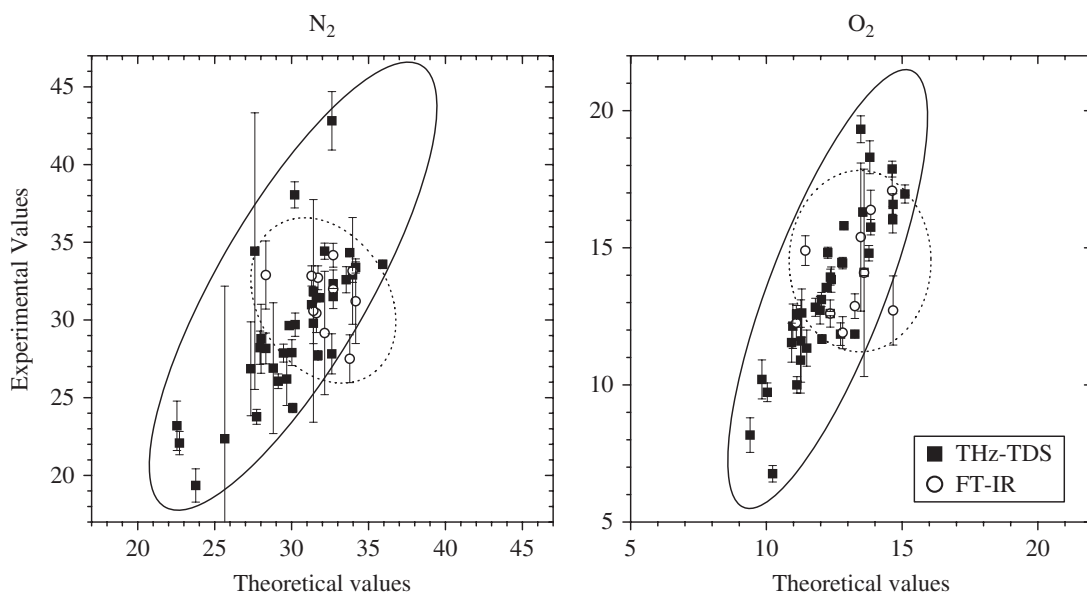

Fig. 7. The correlation plot between the pressure broadening parameters calculated by the theoretical model [15,16] and those obtained from the experiments [17].

result will help in adjusting the models to enable more precise estimation of the spectroscopic parameters of the water vapor.

4.2. The precision of the parameters

To discuss the precision of the obtained pressure broadening parameters, we should be aware of the systematic errors in the linear fittings as exemplified in Fig. 5. In our experiment, two sources are responsible

for the systematic errors, namely the systematic errors from the THz-TDS and those from the sample condition.

Since the sample and the background spectrum were measured separately, the stability of the THz-TDS affects the systematic error of the measurements. The stability of the signal intensity of THz-TDS was estimated using two sets of reference spectra measured in the interval of several hours. The change of the power was estimated to be less than 5% in 2 h. This fluctuation causes the overall shift of ± 0.02 of the baseline in the absorbance, but does not change the line shape of the rotational lines. The fluctuation of the frequency was estimated less than 100 MHz by the shift of the center frequencies in Table 1. The 100 MHz uncertainty of the center frequency corresponds to the 0.01% error of the frequency axis. Thus the signal and frequency fluctuation of THz-TDS does not degrade the precision of the measurements.

On the other hand, the linearity of the signal intensity might cause the systematic errors of the measurements. If the signal output of the THz-TDS detector is not proportional to the THz electric field, the obtained line shape departs from the real line shape. Most probably non-linearity increases gradually as the absorbance increases and it does not cause random error but systematic error of the line parameters. Unfortunately, it is difficult to check the precise linearity of the THz signal intensity by the experiments. We can indirectly confirm the linearity by the fact that the line shape is always well fitted with a Lorentzian line shape function.

Another source of the systematic error is the change of the partial pressure of water vapor in the cell because the change of the partial pressure of water vapor causes a change of the self-pressure broadening line width. Since we cannot monitor and control the adsorption of water vapor in the cell, the amount of water vapor may change during our measurement. In our results, the intensity α increased about 40–50% for H_2O–N_2 and about 20–30% for H_2O–O_2 along with the pressure increase of the foreign gas. If this is due to the change of the partial pressure of water vapor, the increase of self-broadening would cause a slight change of the total line width. To evaluate its possible impact to the pressure broadening parameters, let us assume that the increase of α (40%) of $1_{10} \leftarrow 1_{01}$ of H_2O–N_2 in Table 1 was completely due to the increase of the water vapor amount. Then, a 40% increase of water vapor amount cause a 40% increase of the self-pressure broadening. Assuming that the initial self-pressure broadening equals the intercept of 0.04 GHz, it would increase the line width by 0.02 GHz at 115.2 kPa. Thus, the slope of the plot would increase about 0.2 MHz/kPa. This value corresponds to about 1% of the obtained pressure broadening parameter and is comparable with the error from the linear fitting. Thus, the systematic error of this measurement is probably within about a few percent, and the total error is expected to be less than 3% for typical transitions with good SNR.

5. Conclusion

A White-type multipass cell was built for a THz-TDS system and absorption spectra of water vapor were measured. The pressure broadening parameters γ_{N_2} and γ_{O_2} of pure rotational lines of water vapor were obtained from the plot of HWHM versus the pressure of premixed foreign gas (N_2 and O_2). The pressure broadening parameters of more than 30 lines were obtained for each gas, and their precision was much better than that of conventional results by FT-IR. Due to better SNR of this system, the quantum number dependence of the obtained parameters was observed for the first time.

References

[1] Woolard DL, Loerop WR, Shur MS. Terahertz sensing technology: emerging scientific applications & novel device concepts. Singapore: World Scientific Publishers Co. Inc.; 2004.

[2] Mittleman D. Sensing with terahertz radiation. New York: Springer; 2003.

[3] Han PY, Tani M, Usami M, Kono S, Kersting R, Zhang XC. A direct comparison between terahertz time-domain spectroscopy and far-infrared Fourier transform spectroscopy. J Appl Phys 2001;89:2357–9.

[4] Medvedev IR, Behnke M, Lucia FCD. Fast analysis of gases in the submillimeter/terahertz with "absolute" specificity. Appl Phys Lett 2005;86:154105.

[5] Harmon SA, Cheville RA. Part-per-million gas detection from long-baseline THz spectroscopy. Appl Phys Lett 2004;85:2128–30.

[6] Mittleman DM, Jacobsen RH, Neelamani R, Baraniuk RG, Nuss MC. Gas sensing using terahertz time-domain spectroscopy. Appl Phys B 1998;67:379–90.

[7] Harde H, Cheville RA, Grischkowsky D. Terahertz studies of collision-broadened rotational lines. J Phys Chem A 1997;101:3646–60.

[8] Jacobsen RH, Mittleman DM, Nuss MC. Chemical recognition of gases and gas mixtures with terahertz waves. Opt Lett 1996;21:2011–3.

[9] Cheville RA, Grischkowsky D. Far-infrared terahertz time-domain spectroscopy of flames. Opt Lett 1995;20:1646–8.

[10] Harde H, Katzenellenbogen N, Grischkowsky D. Line-shape transition of collision broadened lines. Phys Rev Lett 1995;74:1307–10.

[11] Harde H, Grischkowsky G. Coherent transients excited by subpicosecond pulses of terahertz radiation. J Opt Soc Am B 1991;8:1642–51.

[12] Harde H, Keiding S, Grischkowsky D. THz commensurate echoes-periodic rephasing of molecular-transitions in free-induction decay. Phys Rev Lett 1991;66:1834–7.

[13] Harde H, Katzenellenbogen N, Grischkowsky D. Terahertz coherent transients from methyl chloride vapor. J Opt Soc Am 1994;11:1018–30.

[14] Rothman LS, Jacquemart D, Barbe A, Benner DC, Birk M, Brown LR, et al. The HITRAN 2004 molecular spectroscopic database. JQSRT 2005;96:139–204.

[15] Gamache RR, Fischer J. Half-widths of $(H_2O)–^{16}O$, $(H_2O)–^{18}O$, $(H_2O)–^{17}O$, $(HDO)–^{16}O$, and $(D_2O)–^{16}O$: I. Comparison between isotopomers. JQSRT 2003;78:289–304.

[16] ⟨http://faculty.uml.edu/Robert_Gamache⟩.

[17] Gasster SD, Townes CH, Goorvitch D, Valero FPJ. Foreign-gas collision broadening of the far-infrared spectrum of water-vapor. J Opt Soc Am B 1988;5:593–601.

[18] Griffiths PR, Haseth JA. Fourier transform infrared spectrometry. 2nd ed. New Jersey: Wiley & Inc.; 2007.

[19] Townes CH, Schawlow AL. Microwave spectroscopy. New York: Dover Publications, Inc.; 1975.

[20] Pickett HM, Poynter RL, Cohen EA, Delitsky ML, Pearson JC, Miller HSP. Submillimeter, millimeter, and microwave spectral line catalog. JQSRT 1998;60:883–90.

[21] Bernath PF. Spectra of atoms and molecules. New York: Oxford University Press; 2005.